第42卷第1期
2023年2月

红外与毫米波学报
J. Infrared Millim. Waves

Vol. 42，No. 1
February，2023

文章编号：1001-9014（2023）01-0111-11

DOI：10. 11972/j. issn. 1001-9014. 2023. 01. 014

An acousto-optic tunable filter spectral measurement method based on compressed sensing

JI Zhong-Peng[1,2]， GUI Yu-Hua[1,2]， LI Jin-Ning[1,2]， TAN Yong-Jian[1,2]， YANG Qiu-Jie[1]， WANG Jian-Yu[1,2*]， HE Zhi-Ping[1,2*]

（1. Key Laboratory of Space Active Opto-Electronics Technology，Shanghai Institute of Technical Physics，Chinese Academy of Sciences，Shanghai 200083，China；
2. University of Chinese Academy of Sciences，Beijing 100049，China）

Abstract：Acousto-Optic Tunable Filter（AOTF）based spectroscopy instruments have been widely applied in biomedical，agricultural，aerospace，and other fields. However，the conventional AOTF spectrometers struggle to achieve increased system luminous flux while maintaining spectral resolution and reducing the number of samples. To address the above problems，this paper proposes an AOTF spectral measurement method based on the compressed sensing（CS）theory. Sparse randomly coded composite optical signal modulation in the spectral domain using the multi-frequency acousto-optic diffraction of AOTF. A modulated composite optical signal is obtained in the spectral domain and recorded sequentially using a single-element detector or a focal-plane detector array. The original spectrum or spectral image data cube is then obtained by using compressed sensing reconstruction algorithms. In order to verify the effectiveness of the present method，we constructed a sensing matrix using the actual measured AOTF spectral response bandwidth data and simulated the effect of compressed sampling and target data reconstruction with the spreading spectrum as the recovery target. The simulation results show that the method can reconstruct the spectral data of 512 wavelength points with 202 compressed samples，and the spectral data sampling rate and compression ratio is 0. 39. Under this sampling rate，the method can recover the spectral curve with high accuracy，and the PSNR index reaches 41. 75 dB，and the SAM and GSAM indexes are 0. 9998 and 0. 9754. With the simultaneous multi-frequency drive，the system optical throughput is improved by a factor of 5 on average. Compared with the traditional wavelength-by-wavelength point scan sampling method，this method can reduce the total number of samples and improve the luminous flux of the system while maintaining the original spectral resolution，and also compressing the spectral data，which is of great importance in the fields of weak signal detection，rapid identification of substances，and spectral data transmission and storage.

Key words：compressed sensing，computational spectroscopy，multi-frequency acousto-optic diffraction，AOTF

基于压缩感知的AOTF光谱测量方法

姬忠鹏[1,2]， 桂裕华[1,2]， 李津宁[1,2]， 谭永健[1,2]， 杨秋杰[1]， 王建宇[1,2*]， 何志平[1,2*]

（1. 中国科学院上海技术物理研究所 空间主动光电技术重点实验室，上海 200083；
2. 中国科学院大学，北京 100049）

摘要：基于声光可调谐滤波器（AOTF）的光谱仪器已经在生物医学、农业、航空航天等领域中广泛应用。然而，传统的AOTF光谱仪很难在保持光谱分辨率和减少采样次数的同时，还实现系统光通量的增加。针对上述问题，本文提出了一种基于压缩感知理论的AOTF光谱测量方法，利用AOTF可多频驱动的特点，在光谱维度上实现稀疏随机编码复合光信号调制，可利用单元或面阵探测器顺次记录完成压缩采样，再通过压缩感知重建算法获得目标光谱曲线或光谱图像数据立方体。为了验证本方法的有效性，我们利用实际测量得到

Received date：2022- 03- 15，**revised date**：2022- 05- 19　　**收稿日期**：2022- 03- 15，**修回日期**：2022- 05- 19

Foundation items：Supported by the National Natural Science Foundation of China（61605231）

Biography：JI Zhong-Peng（1992-），male，Zaozhuang，Shandong，Ph. D. Research area involves spectral imaging method and near-infrared spectroscopy. E-mail：jizhongpeng@aliyun. com

[*] **Corresponding authors**：E-mail：jywang @mail. sitp. ac. cn，hzping@mail. sitp. ac. cn

AOTF光谱响应带宽数据，构建传感矩阵，以展宽光谱为恢复目标，仿真了压缩采样和目标数据重构效果。仿真结果表明，该方法可以通过202次压缩采样，重构得到512个波长点的光谱数据，光谱数据采样率和压缩比为0.39。此采样率下，本方法可以高精度恢复光谱曲线，PSNR指标达到41.75dB，SAM和GSAM指标为0.9998和0.9754。多频同时驱动下，系统光通量平均提升了5倍。与传统逐波长点扫描的采样方式相比，该方法能够在保持原有光谱分辨率的前提下减少总采样次数，提高系统的光通量，同时还压缩了光谱数据，在微弱信号检测、物质快速识别以及光谱数据传输和存储等领域具有十分重要的意义。

关 键 词：压缩感知；计算光谱学；多频声光效应；AOTF

中图分类号：TP751 **文献标识码**：A

Introduction

The acousto-optic tunable filter (AOTF) is a programmable optic filter based on the acousto-optic diffraction effect, easily controlled via radio frequency (RF) signals. Its advantages of flexible wavelength selection, high-frequency optical switching, and solid-state construction provide excellent environmental adaptability. Spectrometers with AOTF as the core spectroscopic element have been successfully applied in the field of in-situ planetary exploration[1-6], astronomical observation[7], urban and industrial pollution monitoring[8], aurora observation[9], atmospheric remote sensing[10-11], surface plasma resonance sensing[12], plume observation, online inspection in the food industry, etc.

When the target light radiation intensity is sufficient, AOTF can take full advantage of quick tuning to achieve fast and effective spectral information acquisition of targets. But under normal circumstances, the intensity of the reflected light from the object is relatively weak, and the energy is relatively low during the measurement. It is necessary to ensure that the detector has sufficient integration time for each measurement. With the conventional AOTF-based spectral-domain scanning sampling method, i. e. wavelength-by-wavelength narrow-band filtering, it takes a long time to acquire the entire spectral data when the number of spectral channels is large[13]. While in some special application scenarios, the acquisition time of a complete spectral data set is strictly limited to ensure the authenticity and validity of the data. For example, in scenarios where there is relative motion between the target and the instrument, the system design usually requires that the full spectral information of the spatial target corresponding to an image element in the image plane needs to be obtained within the time that the image element moves a distance. Again, in a class of application scenarios such as plume observation where the target spectral features change rapidly with time, the system design requires the acquisition of instantaneous spectral data with a guaranteed data signal-to-noise ratio (SNR). In addition, in the field of deep space exploration, due to channel transmission capacity limitations, the massive data obtained by the spectral imaging system often need to be compressed and transmitted. The ground receiving system needs to decompress the data after receiving it for data analysis. Conventional AOTF spectrometers often struggle to meet the needs of these types of applications.

To enable the AOTF spectrometer to increase the system luminous flux, some researchers have developed a multi-frequency mode of operation using the AOTF, where multiple frequencies of RF signals are emitted into the AOTF at the same time, allowing it to output multiple wavelengths of light signals. For a given frequency, the diffraction efficiency (DE) has Gaussian behavior with respect to the applied power. With a multi-channel drive, the AOTF generates a multi-channel passband, resulting in a significant increase in luminous flux stacking. However, Multiplexed AOTF operation is limited by the RF power density that can be accepted by the transducer[14]. There is a limit to the luminous flux increase, and the number of drivers and the share of power per frequency division are mutually constraining. In this multi-channel configuration, different wavelengths of light are coupled together and output to the detector's photosensitive surface. The data obtained directly is the value of a multi-wavelength superposition and cannot be decoupled directly.

In previous researches, various multi-frequency drive methods were proposed. Spanish autonomous tunable filtering system (ATFS) can flexibly configure the spectral resolution and other performance parameters of the AOTF-based spectral imaging system utilizing digital to analog convertor (DAC) multi-frequency drive or direct digital synthesizer (DDS) single-frequency sweep[15]. This approach improves the system's luminous flux, but sacrifices part of the system's spectral resolution because the direct data is obtained after superimposed coupling. The introduction of computational reconstruction mechanisms has guided the strategy of wavelength combination, such as the Hadamard-transform (HT) mechanism[16-17] of combined sampling and back-end decomposition in some studies and appreciable signal-to-noise enhancement is demonstrated. However, this Hadamard encoding method requires the same number of samples as the traditional acquisition method, and this mechanism becomes tricky in the case of the application scenario when the number of wavelength-points to be sampled is large, and does not make good use of the benefits of computational reconstruction.

Since the compressed sensing (CS) theory was put forward[18-19], a variety of computational spectra measurement schemes have emerged. At present, there have been many studies using liquid crystal devices[20], Fabry - Pérot resonant cavities[21], quantum dots[22], and random filter arrays[23], etc. to achieve compressed sensing spectral measurements, with good results. This type of computational spectral measurement system requires back-end inversion recovery reconstruction to obtain the original data after the data are acquired. Its features and great benefits in reducing the number of measurements as well as sampling while performing data compression provide new ideas for improving the performance of conventional systems to suit the needs of specific application scenarios. Compared with the conventional wavelength-by-wavelength scanning sampling method, the sampling method of compressed sensing encoding measurement can reduce the number of samples without reducing the spectral resolution and data SNR, resulting in a reduction in spectral data sampling time.

This paper proposes an AOTF spectral measurement method based on a compressed sensing mechanism. The AOTF multi-passband transmittance encoding curve is used to simulate the compressive sampling process and to reconstruct the obtained data for recovery using three algorithms. The feasibility and effectiveness of the method are demonstrated by means of simulation experiments and numerical analysis.

1 Theoretical analysis

In spectroscopy, the relationship between the spectrum vector $\boldsymbol{x} \in \mathbb{R}^{N \times 1}$ of the light source and the modulated signal $\boldsymbol{y} \in \mathbb{R}^{M \times 1}$ collected by the detector can be expressed as:

$$\boldsymbol{y} = \boldsymbol{A}\boldsymbol{x}, \tag{1}$$

where $\boldsymbol{A} \in \mathbb{R}^{M \times N}$ is a description of the signal sensing process in the spectroscopic system, which is called the sensing matrix. Without loss of generality, the transmittance matrix of a spectral element is denoted by $\boldsymbol{T} \in \mathbb{R}^{N \times N}$. One of the rows is the spectral transmittance curve of the element in one of the measurements, and is expressed as:

$$\boldsymbol{T}_i \in \mathbb{R}^{1 \times N}, i = 1,2,\cdots,N.$$

In conventional spectroscopic instruments, one of the measurement processes in the wavelength-by-wavelength spectroscopic measurement method can be expressed as the inner product of a row of the sensing matrix and the spectral vector, considered as the measured value $\boldsymbol{y}_i$ of a wavelength point λ_i. At this point, the row $\boldsymbol{T}_i$ is generally equivalent to the spectral transmittance curve of a narrow-band filter with a central wavelength λ_i. The number of spectral measurements is also the number of spectral passbands, i. e., $M = N$. Thus, the sensing matrix for conventional measurements can be expressed as: $\boldsymbol{A}_c = \boldsymbol{I}\boldsymbol{T}$, where $\boldsymbol{I}$ is the identity matrix.

Conventionally, narrow bandpass filtering is chosen to perform a wavelength decomposition task. To achieve sufficient spectral resolution, measurements using a certain number of sufficiently narrow passband filters are required. This strategy introduces a trade-off between spectral resolution and light throughput. Meanwhile, the narrow spectral response curve, which limits the light throughput, leads to a limited signal-to-noise ratio[24].

The most distinctive difference between computational and traditional spectroscopic instruments is the sensing matrix. Based on compressed sensing theory, the sensing matrix $\boldsymbol{A} \in \mathbb{R}^{M \times N}, M < N$, implying fewer measurements, is the transmittance matrix of the multi-passband optical devices. By applying multiplexing and computational reconstruction methods[20][21], the fact that multiple spectral peaks are transmitted for each measurement means higher optical throughput, leading to a higher SNR, compared to conventional band-selective spectrometer systems that transmit a single peak.

To solve CS problems, several algorithms were developed[26-28]. A class of reconstruction algorithms estimated the sparse representation $\boldsymbol{s} \in \mathbb{R}^{N \times 1}$ of the spectrum vector $\boldsymbol{x}$ by solving the $l_1$minimization problem:

$$\min \|\boldsymbol{A}\boldsymbol{\Phi}\boldsymbol{s} - \boldsymbol{y}\|_2^2 + \tau\|\boldsymbol{s}\|_1, \tag{2}$$

where τ is a regularization parameter and $\|\cdot\|_p$ the l_p norm.

The reconstructed original spectra can be obtained from the sparse inverse transform:

$$\tilde{\boldsymbol{x}} = \boldsymbol{\Phi}\boldsymbol{s}.$$

where $\boldsymbol{\Phi} \in \mathbb{R}^{N \times N}$ is the sparse inverse transform matrix.

$\boldsymbol{\Phi}$ depends on the sparsity characteristics of the spectral signal and needs to be specified before the measurement is performed. The sparsity of signals and images in a certain transform domain or dictionary has been exploited in many applications in signal and image processing. Analytical sparsifying transforms such as Wavelets and DCT have been widely used in compression standards. And, the problem formulations for learning sparsifying transformations from data have also been proposed[25]. Moreover, the matrix $\boldsymbol{\Psi} = \boldsymbol{A}\boldsymbol{\Phi}$ needs to satisfy the Restricted Isometry Property (RIP) criterion[29].

Under the above framework, a compressed sensing spectral measurement method based on AOTF is proposed in this paper.

The spectral measurement method based on AOTF can be configured to acquire a single narrowband spectrum, a composite multispectral image, or a broadband passband. This flexibility is achieved through the use of an AOTF driven by the programmable RF signal generator. The AOTF acts as an optical diffraction element and its output wavelengths are selected by RFs applied to it. The RF driver based on a high-speed DAC is capable of synthesizing arbitrary composite RF waveforms from a combination of sinusoidal signals.

By varying composite RF waveforms of the designed driver, the AOTF generates the spectral masks given by the designed matrix. Without changing the optical path setup of the conventional AOTF spectroscopy instrument, the compressive sampling process under the compressed sensing framework is realized. The optical signal is modulated in the spectral domain and the detector is used to record the modulated composite optical signal in sequence. Finally, the original spectrum is obtained with the compressive sensing reconstruction algorithm.

As shown in Fig. 1, a row of the sensing matrix $\boldsymbol{A}$ is inner-produced with the original spectral signal $\boldsymbol{x}$ to obtain an element of the measured value $\boldsymbol{y}$. This is a compressive sampling process. The measurements obtained

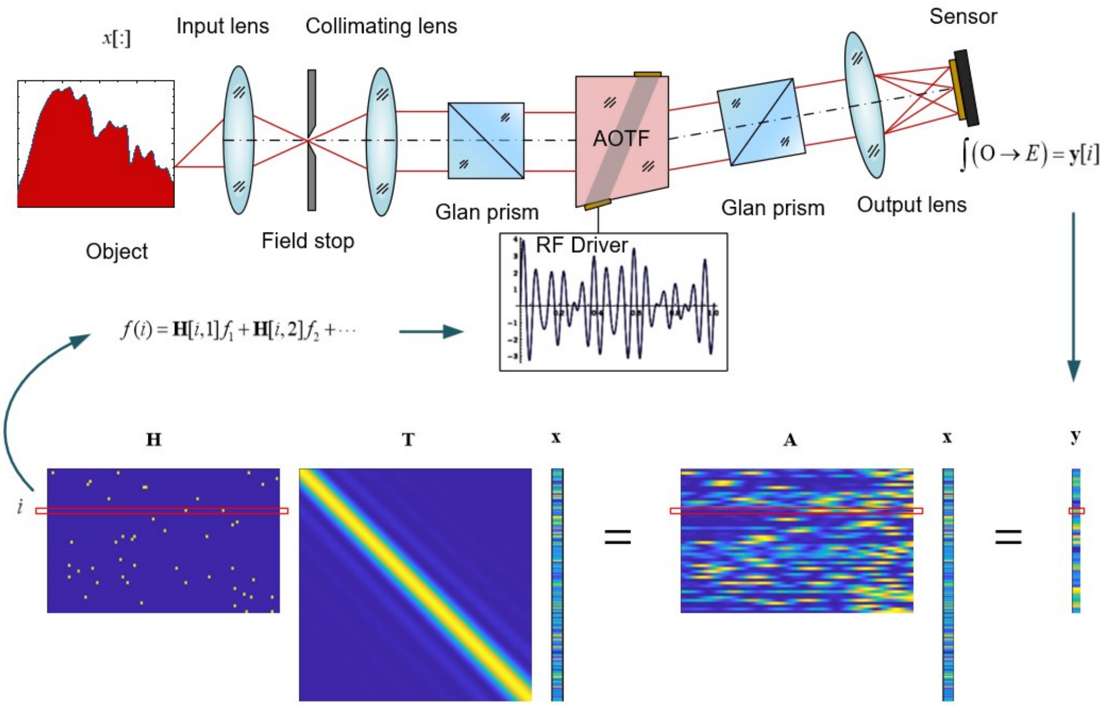

Fig. 1 Compressive sampling based on AOTF
图1 声光编码压缩采样

by compressive sampling represent the superimposed signal intensity of a particular combination of wavelengths in the spectral domain. This coding according to the sensing matrix ***A*** requires that the wavelength combinations of the actual diffracted light from the AOTF match those determined by the designed matrix ***H***.

Based on this combination of wavelengths and the frequency table corresponding to the chosen AOTF device, the frequency combination required for each drive can be obtained. During the actual measurement, the drive subsystem needs to be able to drive the AOTF in a flexible and stable sequence according to a set series of frequency combinations, while the back-end detector subsystem records the measured values simultaneously. By measuring the spectrum of the light source and the diffracted light spectrum of the AOTF crystal, the overall equivalent spectral transmittance of the spectroscopic system can be obtained. Measuring the actual equivalent spectral transmittance allows verification that the actual modulation effect of the system is consistent with the designed measurement matrix.

For AOTF, the intrinsic momentum matching condition is highly selective in collimated light with fully collimated acoustic waves. However, due to the limited length of the transducer, the spectral resolution and bandpass shape are usually influenced by the diffraction of the acoustic field[7]. This results in a $\sin c^2$ distribution of acoustic energy in the crystal in the plane of the optical axis, where $\sin c(x) = \sin(\pi x)/\pi x$.

Defining the acoustic wave length $\Lambda = V_a/f$, the spreading due to the momentum mismatch resulting from different directions of the acoustic wave vector at slightly different optical wavelengths, the full width at half maximum $FWHM(\Delta\lambda_{FW})$ of the passband can be approximated as Eq. (3).

$$\Delta\lambda_{FW} = \frac{1.8\pi\lambda_0^2}{b_\lambda L \sin^2\Theta_i}. \tag{3}$$

The bandpass shape of the homogeneous transducer and collimated input light is:

$$\boldsymbol{T}_\lambda = T_0 \sin c^2\left(0.886\frac{\lambda - \lambda_0^2}{\Delta\lambda_{FW}}\right). \tag{4}$$

Eq. (4) describes the passband transmittance function of AOTF narrowband filtering at a specific wavelength. The transmittance functions at all wavelengths to be sampled are combined to form the matrix ***T***.

In our approach, the broadened spectrum ***Tx*** is chosen instead of ***x*** as the target for reconstruction recovery.

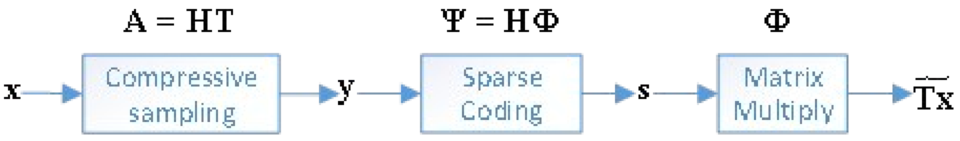

Fig. 2 Sparse-reconstruction Compressed Sensing System model
图2 稀疏重构压缩感知系统模型

In Fig. 2, we show the whole data flow process:

a. The light spectral distribution is modulated and multiplexed by AOTF to obtain the measured value $\boldsymbol{y}$;

$$\boldsymbol{y} = \boldsymbol{Ax} = \boldsymbol{HTx}.$$

b. Using the broadened spectrum $\boldsymbol{Tx}$ sparsity feature, the sparse transformation matrix $\boldsymbol{\Phi}$ is determined and combined with the designed matrix $\boldsymbol{H}$ to obtain the matrix $\boldsymbol{\Psi}$, which is required to satisfy the RIP criterion.

$$\boldsymbol{\Psi} = \boldsymbol{H\Phi}.$$

Using $\boldsymbol{y}$, $\boldsymbol{\Phi}$ and $\boldsymbol{A}$, solve Eq. (2) to obtain the sparse representation $\boldsymbol{s}$.

c. A matrix calculation is performed to obtain the reconstructed target broadened spectrum.

$$\widetilde{\boldsymbol{Tx}} = \boldsymbol{\Phi s}.$$

In the next section, simulation experiments are performed using the measured data of selected AOTF devices, and the spectrum reconstruction from a semi-simulated experiment is evaluated for similarity to the target.

2 Numerical analysis and simulation experiments

For the simulation experiments, the measurement spectral range was selected to be 600~855. 5 nm with a wavelength interval of 0. 5 nm and a total of 512 spectral bands.

$$N = 512$$

The sensing matrix $\boldsymbol{A}$ is constructed from the selected measurement matrix $\boldsymbol{H}$ with elements 0 and 1 and the single wavelength filtered response passband matrix $\boldsymbol{T}$ of the AOTF at each wavelength point of the spectral signal to be measured, expressed as $\boldsymbol{A} = \boldsymbol{HT}$.

In order to obtain a rational $\boldsymbol{T}$, the bandwidth of the spectral response curve of the AOTF crystal corresponding to different diffraction center wavelengths was first measured. A HORIBA iHR 320 spectrometer was used to measure the diffracted light from a tungsten halogen lamp through the AOTF. Based on the relationship between the driving frequency of the AOTF and the diffraction wavelength, the frequency corresponding to one of the wavelengths to be measured was set. The diffracted light spectrum curve was then obtained using the spectrometer by fine-step scanning. The full width at half maximum of the curve was then used as the spectral resolution data for the AOTF at the wavelength. This procedure was repeated five times over the entire working spectral range to obtain all data.

Using the measured spectral resolution data of the selected AOTF device, as shown in Table 1, the full width at half maximum $FWHM\left(\Delta\lambda_{FW}\right)$ of the passband at all wavelength-points in the operating spectral range is fitted according to the quadratic function of Eq. (3), and the spectral passband $\boldsymbol{T}_{\lambda}$ at each wavelength point required is generated by combining Eq. (4). 512 corresponding narrow passbands were generated to construct the matrix $\boldsymbol{T}$.

Table 1 Spectral resolution data of the selected AOTF device
表1 所选AOTF器件的光谱分辨率测量数据

Wavelength/nm	Driver frequency/MHz	Diffracted efficiency	FWHM/nm
600	121. 8	0. 735	5. 401
650	110. 5	0. 935	6. 2
700	101. 1	0. 882	7. 8
750	93. 3	0. 727	9. 4
800	86. 7	0. 522	10. 999

For AOTF spectroscopic instrumentation systems based on AOTF spectroscopy, the conventional measurement mode in which a single frequency drives the AOTF equally spaced non-ideal narrow-band filtering for target spectral sampling is equivalent to the discrete sampling of the AOTF measurement spectrum $\boldsymbol{Tx}$. The coded measurements operate on spectral data, and each compressed sample can be equated to a linear combination of specific multiple single wavelength samples. The linear combination method is determined by the measurement matrix $\boldsymbol{H}$. Considering the AOTF device and transducer energy threshold limits and the drive system output power, the maximum number of frequencies in a single drive needs to be strictly limited.

As mentioned above, $\boldsymbol{\Psi} = \boldsymbol{H\Phi}$ needs to satisfy the RIP criterion. The hierarchical condition for the RIP property is that the measurement matrix and the sparse transform base are uncorrelated, whereby the optimal measurement matrix can be selected and generated based on hardware metrics and spectral sparsity properties. Common random matrices include random Gaussian measurement matrices, random Bernoulli matrices, partially orthogonal matrices, sparse random matrices, etc. Considering the reconstruction recovery effect and hardware implementation feasibility, the Sparse Random Matrix (elements 0 and 1) is chosen as the measurement matrix $\boldsymbol{H}$.

The RIP criterion is easily satisfied due to the Sparse Random Matrix with the determined sparse transformation matrix extremely incoherence. It has been demonstrated that given a signal $\boldsymbol{s}$ sparsity of K, the minimum number of measurements:

$$M \approx 4K \text{ or } M \geqslant K\log_2\left(\frac{N}{K}\right). \tag{5}$$

Since the sparsity of the target broadened spectrum $\boldsymbol{Tx}$ is unknown, we set the number of compressing measurements to 202 for this simulation experiment.

$$M = 202$$

Therefore, if it can be reconstructed almost perfectly, the compression ratio is 0. 39.

During a conventional raster spectral acquisition, only one channel of the AOTF is turned on and tuned in frequency to probe a single different wavelength at each acquisition ($\mathbf{A}_{ci}$). In sensing matrix $\mathbf{A}$ for acousto-optic coded sampling based on compressed sensing, several channels of the AOTF are turned on simultaneously in each acquisition. The additional passbands brought about an increase in optical throughput.

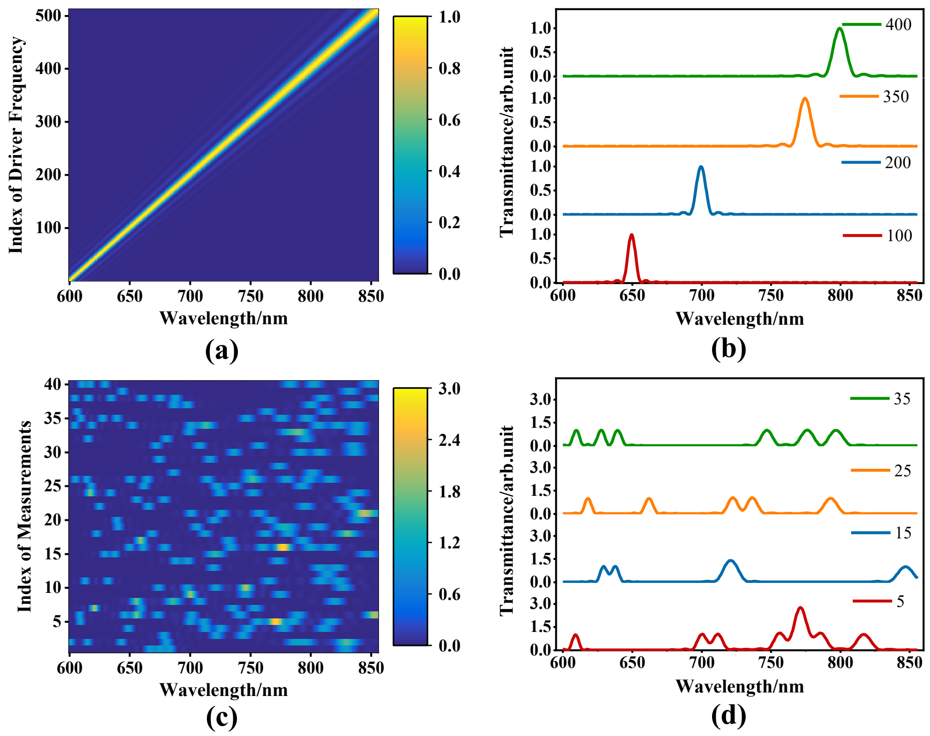

Fig. 3 Sampling matrix visualization (a) sensing matrix $\mathbf{A}_c$ for conventional wavelength-by-wavelength point sampling, each row represents the spectral transmittance data of AOTF driven by a single frequency, (b) four of the spectral transmittance curves, (c) sensing matrix **A** (50 of 202) for acousto-optic coded sampling based on compressed sensing; each row represents the spectral transmittance of the system at a given state of AOTF, (d) four of the equivalent spectral transmittance curves

图3 采样矩阵的可视化(a)传统逐波长点采样的传感矩阵Ac,每一行代表单频驱动下的AOTF的光谱透过率数据,(b)其中四条光谱透过率曲线,(c)压缩感知声光编码采样的传感矩阵A(202中的50个),每一行代表系统在AOTF给定状态下的光谱透过率,(d)其中四条等效光谱透过率曲线

Many studies[15-16][30] have demonstrated that the multi-passband of an AOTF driven by multiple frequencies simultaneously is equivalent to the mathematical superposition of the narrow passbands when the AOTF is driven by each single frequency separately, under reasonable settings. Based on this assumption, a mathematically linear combination of the narrow passbands of different single-frequency driven AOTFs was also used in this paper to characterize the broad passbands when driven by multiple frequencies simultaneously.

The number of simultaneously driven frequencies determines the magnitude of the luminous flux in the passband. Since the sparse random matrix $\boldsymbol{H}$ chosen for the simulation, with the sparsity of the columns set to 2, the number of driving RFs per row, also called, each compressed measurement, is randomly distributed between 1 and 11, and the average number of simultaneous driving RFs for all 202 measurements is 5, so the system light throughput is considered to be increased by a factor of 5.

Fig. 3 shows the heat map of the normalized equivalent spectral transmittance (50 of the 202), which are denoted as $\boldsymbol{A}$ in the simulation, and the spectral response curves corresponding to the four measurements in it. The simulation uses a certain generated Sparse Random Matrix with the maximum number of wavelengths that need to be sampled simultaneously for a single sampling in all rows is 11.

As mentioned earlier, the maximum number of simultaneously driven RFs is limited by the RF power density that can be accepted by the transducer. The effective driving of 16 simultaneous passbands has been verified in previous studies[30]. Therefore, it is easier to implement in hardware compared to other measurement matrices. For example, a partial Hadamard matrix, which requires the number of simultaneously turned-on passbands to be typically half of the original total number of samples, is difficult be implemented in hardware at this stage.

The target spectrum is selected as the broadened spectrum of the Hg-Ne-Ar spectral calibration source of the *IntelliCal* series from Princeton Instruments (PI), USA, after the conventional sampling by AOTF.

The red line spectrum shown in Fig. 4(a) is the original emission spectrum of the source, and the blue spectral curve is the conventional measured spectrum of AOTF, which is represented as $\boldsymbol{x}$ and $\boldsymbol{Tx}$, respectively, in the simulation. The measured values obtained from 202 compressive measurements are shown in Fig. 4(b) which are denoted as $\boldsymbol{y}$ in the simulation.

Our approach, choosing $\boldsymbol{Tx}$ as the compressed sensing reconstruction target instead of $\boldsymbol{x}$, brings multifaceted benefits. Including, the broadened spectrum is naturally sparse, the measurement matrix can be chosen randomly without introducing fixed $\boldsymbol{T}$, and the spectral resolution can be unambiguous (remain unchanged with the one by conventional methods).

For some application scenarios where the target data to be detected does not require higher spectral resolution, our method can be designed with a random measurement matrix for a given spectral resolution so that performance close to the theoretical minimum number of measurements can be achieved for a given sparse transformation. This minimizes sampling costs.

As mentioned before, the size of the sparsity after the sparse transformation determines the minimum number of measurements. Hence, the most suitable sparse transform for the measured signal is worth to be explored. Without loss of generality, one of the sparse transforms is selected in this paper for simulation and verification. If a better sparse transform is replaced in the future, it will be possible to further reduce the number of measurements while achieving a relatively perfect recovery.

In this paper, the sparsifying transform used for reconstructing the broadened spectra $\boldsymbol{Tx}$ is from the family of orthogonal Daubechies wavelet. The Discrete Wavelet Transform (DWT) matrix $\boldsymbol{W}$ is generated by performing a level 3 decomposition of the signal using the db6 wavelet. The sparse transformation matrix $\boldsymbol{\Phi}$ is obtained by solving the inverse matrix for $\boldsymbol{W}$.

$$\boldsymbol{\Phi} = INV(\boldsymbol{W})$$

At this point, we obtained $\boldsymbol{A}$, $\boldsymbol{y}$ and $\boldsymbol{\Phi}$. The next step is the signal reconstruction simulation.

To solve the optimization problem as in Eq. (2), reconstruction simulations were performed using the L1-MAGIC toolbox[26] and the l1_ls solver [27], respectively. The Orthogonal Matching Pursuit (OMP) algorithm[28] was also applied for reconstruction recovery.

The iterative optimization yielded $\boldsymbol{s}$, and then the matrix multiplication calculation with the sparse transformation matrix $\boldsymbol{\Phi}$ was performed to obtain the reconstructed spectral signal $\widetilde{\boldsymbol{Tx}}$.

Fig. 5 (b) visualizes the comparison of the reference spectral curve $\boldsymbol{Tx}$ and the three reconstructed spectral curves $\widetilde{\boldsymbol{Tx}}$ generated by L1-MAGIC, l1_ls, and OMP. A randomly selected part of the area is enlarged to show that the curves match relatively well. Almost perfect recovery was achieved, both in terms of the overall curve trend and the shape, area, and position of the spectral emission peaks. All three algorithmic tools availably completed the refactoring task.

Since the sparse inverse transformation from the wavelet domain sparse signal to the original spectral intensity signal is not a perfect recovery. We also examined the difference between the reconstructed sparse signal before the sparse inverse transformation by matrix multiplication and the actual sparse transformation of the broadened spectrum.

The actual sparse signal in the wavelet domain of the AOTF broadened spectrum $\boldsymbol{Tx}$ is denoted as $\boldsymbol{s}_0$.

Fig. 5 (a) shows the comparison of the reference sparse signal $\boldsymbol{s}_0$ in the wavelet transform domain and the sparse representation $\boldsymbol{s}$ obtained by the three algorithms.

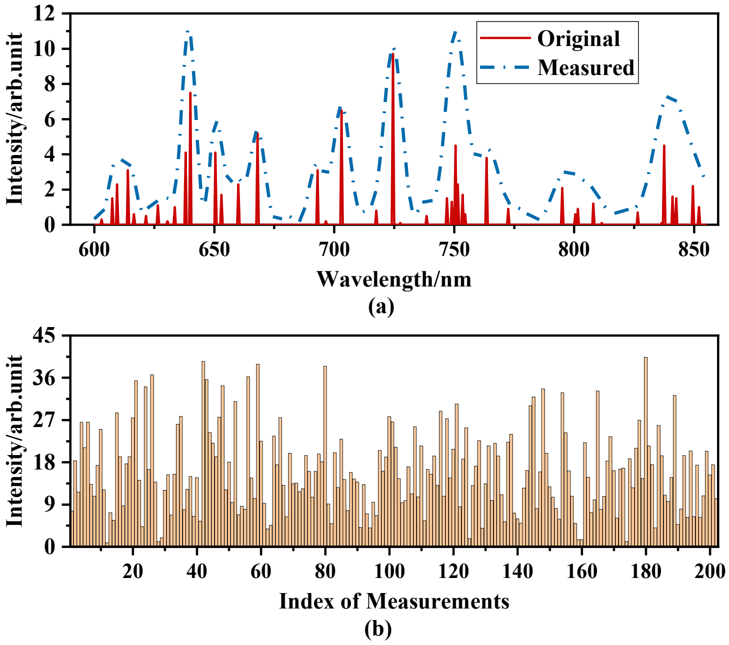

Fig. 4 Comparison of the measured values obtained from the two methods
图4 两种方式直接得到的测量值对比

A randomly selected part of the area is also enlarged to show that the curves match relatively well.

Quantitative evaluation of reconstruction accuracy[21-22] can be done using the peak signal-to-noise ratio (PSNR). PSNR is a scientific parameter for the measurement of the similarity of two signals, which is calculated as follows:

$$\mathrm{PSNR} = 10\log_{10}\left(\frac{MAX_I^2}{MSE}\right), \quad (6)$$

where MAX_I is the maximum intensity value of the signals and MSE is Mean Squared Error between the reference and reconstruction signal.

The peak signal-to-noise ratios of the three different reconstruction algorithms were calculated in the sparse and spectral domains, respectively. As shown in Table 2. We can see that the l1_ls solver obtains the highest PSNR, which means the highest reconstruction accuracy with the least distortion. In general, a PSNR above 40 dB means that the signal quality is pretty good (i. e. , very close to the original signal). And, PSNR between 30-40dB usually means that the signal quality is good (i. e. distortion is detectable but acceptable). Thus, the recovery of L1-MAGIC and l1_ls is almost perfect, while the recovery of OMP is also acceptable.

Moreover, as expected, the accuracy of reconstruction recovery in the sparse domain is much higher before undergoing sparse inverse transformation. PSNR in the sparse domain even exceeds 50dB.

Table 2 PSNR of three different reconstruction algorithms

表2 三种重构算法的峰值信噪比

Solvers	PSNR in the spectral domain	PSNR in the sparse domain
L1-MAGIC	41. 4802	50. 2913
l1_ls	41. 7517	50. 5628
OMP	36. 8563	45. 6674

In Paper[31], it is indicated that the fidelity of spectral restoration can be evaluated using the Spectral Angle Model (SAM) and Gradient Spectral Angle Model (GSAM) metrics. The SAM and GSAM were calculated for the three reconstruction algorithms, as shown in Table3.

The simulation results show that with the above settings, only 202 measurements successfully reconstructed

Table 3 SAM and GSAM of three different reconstruction algorithms in the spectral domain

表3 三种重构算法的光谱保真度指标SAM和GSAM值

Solvers	SAM	GSAM
L1-MAGIC	0. 9997	0. 9731
l1_ls	0. 9998	0. 9754
OMP	0. 9561	0. 8868

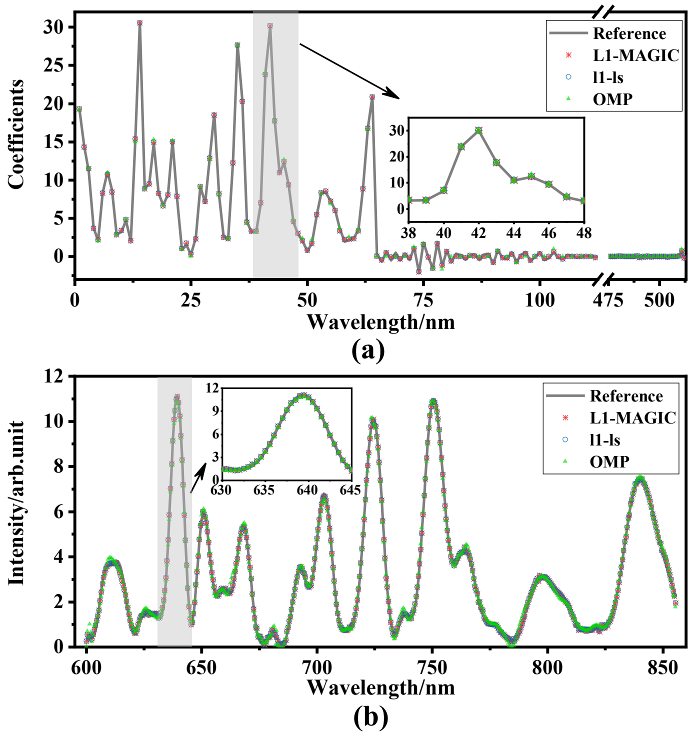

(a)

(b)

Fig. 5 Spectral reconstruction results of L1-MAGIC, l1_ls, and OMP, from 202 measurements of 512 spectral bands (600~855. 5 nm), (a) reference signal vs reconstruction signals in the wavelet transform domain, (b) reference signal vs reconstruction signals in the spectral domain

图5 三种算法 L1-MAGIC、l1_ls 和 OMP 使用202次测量值重建512个波长点数据(600~855. 5 nm)的结果,(a) 小波变换域中的参考信号与重建信号对比,(b) 光谱域中的参考信号与重建信号的对比

the target data of 512 points almost perfectly by the method proposed in this paper.

In the above Hg-Ne-Ar spectral curve simulation, since the real spectrum of the Hg-Ne-Ar source is known, the response $\boldsymbol{T}$ matrix of the AOTF spectral instrument can be used to broaden the real spectrum to obtain the measured spectrum $\boldsymbol{Tx}$. Then the compression sampling simulation and reconstruction recovery simulation were completed by combining the measurement matrix $\boldsymbol{H}$ and the sparse transformation matrix $\boldsymbol{\Phi}$. To further validate the method in this paper, simulations were next performed using data from a spectral database with richer features.

When using the data from the spectral library for simulation, since the data from the spectral library obtained from the actual acquisition of the typical instruments, the broadening characteristics of the instruments such as the wavelength position data of each channel and the FWHM of each channel were recorded in addition to the detailed reflectance spectral curve data of different geographical targets.

In the simulation, it was assumed that the spectral radiation energy of the illumination source of the feature target is flat in the working spectral range, at which time the reflectance spectral curve in the spectral library can be regarded as the spectral curve of the reflected light entering the instrument in the simulation. Therefore, the spectral library data can be considered as $\boldsymbol{Tx}$. As can be seen from the previous simulation, the $\boldsymbol{T}$ matrix is only involved in the process of obtaining $\boldsymbol{Tx}$. With the known $\boldsymbol{Tx}$, the compressed sampling simulation can be completed by setting $\boldsymbol{H}$ only. In the evaluation of reconstruction recovery results, $\boldsymbol{Tx}$ was also directly used as the target reference spectrum without explicit $\boldsymbol{T}$ matrix. Therefore, the spectral library data were simulated throughout with no $\boldsymbol{T}$ involved. Since the OMP recovery results in the previous simulations were relatively poor, while the l1-MAGIC and l1-ls algorithms worked better, the following simulations were reconstructed using these two algorithmic tools.

The reflectance spectrum data for the 75 materials used in the simulations are located in the USGS_Spectral_Library_Version_7 spectral library under the veg_1dry and veg_2grn categories. For each spectrum data, a total of 512 wavelength points in the spectral range of 0.714~2.5 μm were intercepted as the recovery target. Using the same measurement matrix $\boldsymbol{H}$ as in the previous section, with $M = 202$ and $N = 512$, the direct simulation results are presented below.

A statistical analysis of the spectral fidelity metrics

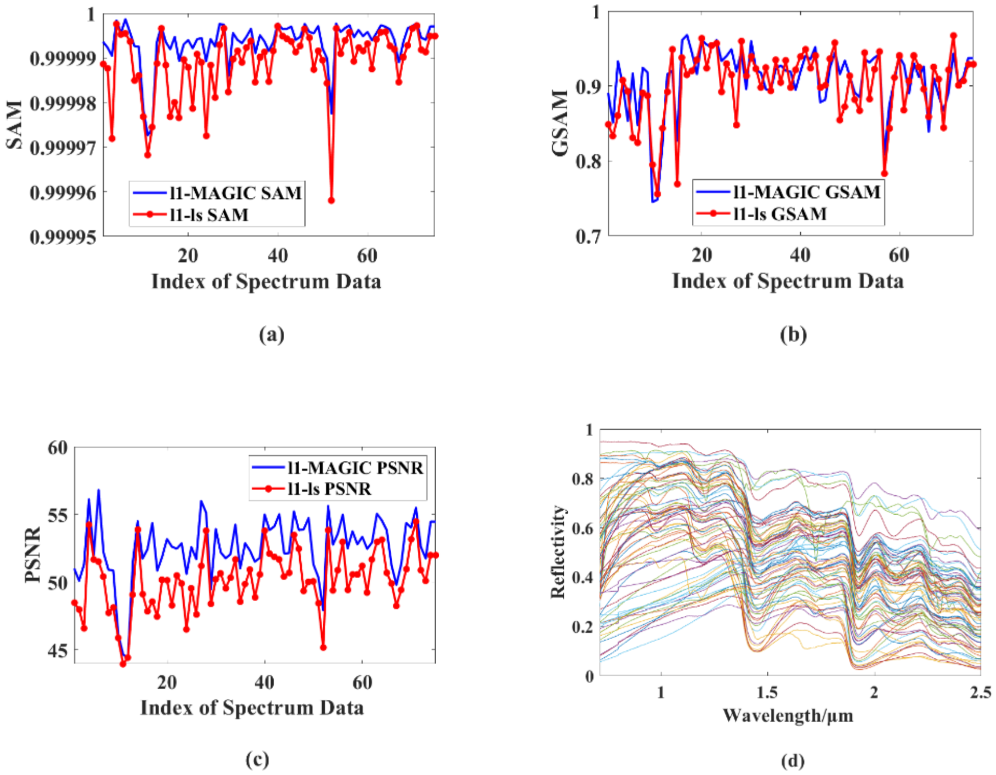

Fig.6 Reconstruction results of spectrum data of 75 materials in the spectral library. (a) comparison of SAM metrics for the recovery results of the two reconstruction algorithms, (b) comparison of GSAM metrics for the recovery results of the two reconstruction algorithms, (c) comparison of PSNR metrics for the recovery results of the two reconstruction algorithms. (d) spectral reflectance curves of 75 materials (0.714~2.5 μm)

图6 光谱库中75种材料的光谱数据的重构结果,(a)两种重构算法恢复结果的SAM指标对比,(b) 两种重构算法恢复结果的GSAM指标对比,(c) 两种重构算法恢复结果的PSNR指标对比,(d) 75种材料的光谱反射率曲线（0.714~2.5 μm） was performed and is displayed in Table 4. The results show that the average PSNR can reach 52.54, and the average SAM and average GSAM are 1.000 and 0.9091, respectively, when the compressed sampling rate is no higher than 0.4.

Table 4 The average of spectral fidelity metrics
表4 光谱保真度指标的平均值

Solvers	PSNR	SAM	GSAM
L1-MAGIC	52.5477	1.0000	0.9091
l1_ls	50.1489	1.0000	0.9006

This method chooses the broadened spectrum by conventional measured as the sparse transform target so that the final spectral data obtained by the method is consistent with the spectral resolution characteristics of the spectral data obtained by the conventional AOTF spectrometer. The compressive sampling process reflects the system's luminous flux advantage and reduced sampling points. At the same time, the new form of transmittance coding model based on AOTF does not change the original optical path setup and does not need additional coding optical components.

It can be seen from the results that the scheme can achieve sufficient recovery accuracy with a reasonable computational overhead. The simulation experimental results verify that the selection of the measurement matrix and the overall data flow design of the system in this paper can reach the goal of coding for compressed sensory spectral measurements. This simulation experiment did not introduce noise, and further studies based on this can take noise into account.

3 Conclusions

In this paper, we propose an AOTF spectral measurement method based on compressive sensing, and conduct simulations to verify the feasibility of computational spectral measurement through AOTF. Simulation results show that the method proposed in this paper can achieve fast acquisition of target spectral data with fewer measurements and higher luminous flux for signal sampling, and simultaneous data compression in the spectral domain to accurately reconstruct signals at 39% or even fewer measurements. Based on the method proposed in this paper, the acousto-optic multi-RF drive source and acousto-optic encoded spectral measurement system can be developed, and it is expected that the number of measurements can be further reduced, the reconstruction accuracy and the reconstruction calculation speed can be improved by selecting a better sparse strategy and a reconstruction algorithm with better performance. This method will provide a reference for the acousto-optic encoded spectral detection system based on compressive sensing and broaden the application of compressive sensing theory in the field of spectral detection.

References

[1] HE Zhiping, *et al*. Operating principles and detection characteristics of the Visible and Near-Infrared Imaging Spectrometer in the Chang'e-3[J]. *RAA*, 2014, **14**(12): 1567-1577.

[2] HE Zhiping, *et al*. Visible and near-infrared imaging spectrometer and its preliminary results from the Chang'E 3 project[J]. *Review of Science Instruments*, 2014, **85**, 083104.

[3] C.L. Li, Z.D. Wang, R. Xu, *et al*. ‘‘The Scientific Information Model of Chang'e-4 Visible and Near-IR Imaging Spectrometer (VNIS) and In-Flight Verification’’. *Sensors*. 2019. **19**(12): E2806.

[4] Z.P. He, C.L. Li, R. Xu, *et al*. ‘‘Spectrometers Based on Acousto-Optic Tunable Filters for In-Situ Lunar Surface Measurement’’. *J. Appl. Remote Sens*. 2019. **13**(2): 027502.

[5] He, Zhiping, et al. "Measurement and Correction Model for Temperature Dependence of an Acousto-Optic Tunable Filter (AOTF) Infrared Spectrometer for Lunar Surface Detection." *Applied Spectroscopy*, vol. **74**, no. 1, 2020, pp. 81 – 87.

[6] Chanover N J, Glenar D A, Voelz D G, *et al*. An AOTF-LDTOF spectrometer suite for in situ organic detection and characterization [C]//2011 Aerospace Conference. IEEE, 2011: 1-13.

[7] Glenar D A, Hillman J J, Saif B, *et al*. Acousto-optic imaging spectropolarimetry for remote sensing[J]. *Appl Opt*, 1994, **33**(31): 7412-7424.

[8] Dekemper E, Vanhamel J, Van Opstal B, *et al*. The AOTF-based NO_2 camera[J]. *Atmospheric Measurement Techniques*, 2016, **9**(12).

[9] Vanhamel J, Dekemper E, Berkenbosch S, *et al*. Novel acousto-optical tunable filter (AOTF) based spectropolarimeter for the characterization of auroral emission[J]. *Instrumentation Science & Technology*, 2020: 1-13.

[10] Dekemper E, Vanhamel J, Kastelik J C, *et al*. New AOTF-based instrumental concepts for atmospheric science[C]//Fourteenth School on Acousto-Optics and Applications. International Society for Optics and Photonics, 2019, **11210**: 112100S.

[11] Dekemper E, Loodts N, Van Opstal B, *et al*. Tunable acousto-optic spectral imager for atmospheric composition measurements in the visible spectral domain[J]. *Applied optics*, 2012, **51**(25): 6259-6267.0

[12] Zeng Y, Wang L, Wu S Y, *et al*. Wavelength-scanning SPR imaging sensors based on an acousto-optic tunable filter and a white light laser[J]. *Sensors*, 2017, **17**(1): 90.

[13] Gat N. Imaging spectroscopy using tunable filters: a review[C]// Wavelet Applications VII. International Society for Optics and Photonics, 2000, **4056**: 50-64.

[14] Davies W S. Design and fabrication of acousto-optic devices[J]. *Optics and Lasers in Engineering*, 1994, **21**: 249-250.

[15] Vila-Francés, Joan, et al. "Design of a Configurable Multispectral Imaging System Based on an AOTF." *IEEE Transactions on Ultrasonics Ferroelectrics and Frequency Control*, vol. **58**, no. 1, 2011, pp. 259 – 262.

[16] Genchi L, Bucci A, Laptenok S P, *et al*. Hadamard-transform spectral acquisition with an acousto-optic tunable filter in a broadband stimulated Raman scattering microscope[J]. *Optics Express*, 2021, **29**(2): 2378-2386.

[17] Hammaker R, DeVerse R, Asunskis D, *et al*. Hadamard Transform Near-Infrared Spectrometers[M]. 2006.

[18] Gehm M E, John R, Brady D J, *et al*. Single-shot compressive spectral imaging with a dual-disperser architecture[J]. *Optics express*, 2007, **15**(21): 14013-14027.

[19] Wagadarikar A, John R, Willett R, *et al*. Single disperser design for coded aperture snapshot spectral imaging[J]. *Applied optics*, 2008, **47**(10): B44-B51.

[20] August, Yitzhak, and Adrian Stern. "Compressive Sensing Spectrometry Based on Liquid Crystal Devices." *Optics Letters*, vol. **38**, no. 23, 2013, pp. 4996 – 4999.

[21] Oiknine, Yaniv, et al. "Compressive Sensing Resonator Spectroscopy." *Optics Letters*, vol. **42**, no. 1, 2017, pp. 25 – 28.

[22] Bao, Jie, and Moungi G. Bawendi. "*A Colloidal Quantum Dot Spectrometer*." *Nature*, vol. **523**, no. 7558, 2015, pp. 67 – 70.

[23] Oliver J., *et al*. "Filters with Random Transmittance for Improving Resolution in Filter-Array-Based Spectrometers." Optics Express, vol. **21**, no. 4, 2013, pp. 3969 – 3989.

[24] Song, Hongya & Zhang, Wenyi & Li, Haifeng & Liu, Xu. (2020). Review of compact computational spectral information acquisition systems. *Frontiers of Information Technology & Electronic Engineering*. 21. 10.1631/FITEE.1900266.

[25] Ravishankar, Saiprasad & Bresler, Yoram. (2013). Learning Sparsifying Transforms. *IEEE Transactions on Signal Processing*. 61. **1072**-1086. 10.1109/TSP.2012.2226449.

[26] Candès, Emmanuel & Romberg, Justin & Tao, Terence. (2006). Stable Signal Recovery from Incomplete and Inaccurate Measurements. *Communications on Pure and Applied Mathematics*. 59. 10. 1002/cpa.20124.

[27] Kim, Seung-Jean & Koh, K. & Lustig, M. & Boyd, Stephen & Gorinevsky, Dimitry. (2008). An Interior-Point Method for Large-Scale L1-Regularized Least Squares. *Selected Topics in Signal Processing*, *IEEE Journal of*. 1. **606** - 617. 10.1109/JSTSP. 2007. 910971.

[28] Joel A Tropp. Greed is good: Algorithmic results for sparse approximation. *IEEE Transactions on Information theory*, **50**(10): 2231 - 2242, 2004.

[29] Candès, Emmanuel. (2008). The restricted isometry property and its implications for compressed sensing. *Compte Rendus de l'Academie des Sciences*. 346. **589**-592. 10.1016/j.crma.2008.03.014.

[30] Neelam Gupta and Dennis R. Suhre, "Notch filtering using a multiple passband AOTF in the SWIR region," *Appl. Opt. 55*, 7855-**7860** (2016)

[31] LIU Shi-Jie, LI Chun-Lai, XU Rui, *et al*. High-precision algorithm for restoration of spectral imaging based on joint solution of double sparse domains[J], *J. Infrared Millim. Waves*, 2021, **40**(5): 685~695.（刘世界,李春来,徐睿,等. 基于双稀疏域联合求解的高精度光谱恢复算法,**红外与毫米波学报**). 2021,**40**(5):685~695.